

RESEARCH ARTICLE

# Dissociation Between Neuronal and Astrocytic Calcium Activity in Response to Locomotion in Mice

Anna Fedotova<sup>1,2</sup>, Alexey Brazhe<sup>1,2</sup>, Maxim Doronin<sup>2,3</sup>, Dmytro Toptunov<sup>4</sup>, Evgeny Pryazhnikov<sup>4</sup>, Leonard Khiroug<sup>4</sup>, Alexei Verkhratsky<sup>5,6,7,8,\*</sup>, Alexey Semyanov<sup>1,2,3,9,\*</sup>

<sup>1</sup>Faculty of Biology, Moscow State University, Moscow 119991, Russia, <sup>2</sup>Department of Molecular Neurobiology, Shemyakin-Ovchinnikov Institute of Bioorganic Chemistry RAS, Moscow 117997, Russia, <sup>3</sup>College of Medicine, Jiaying University, Jiaying, Zhejiang Province, 314001, China, <sup>4</sup>Neurotar, Viikinkaari 4, FI-00790 Helsinki, Finland, <sup>5</sup>Department of Forensic Analytical Toxicology, School of Forensic Medicine, China Medical University, Shenyang 110122, China, <sup>6</sup>Faculty of Biology, Medicine and Health, The University of Manchester, Manchester M13 9PL, UK, <sup>7</sup>Achucarro Centre for Neuroscience, IKERBASQUE, Basque Foundation for Science, 48011 Bilbao, Spain, <sup>8</sup>Department of Stem Cell Biology, State Research Institute Centre for Innovative Medicine, LT-01102 Vilnius, Lithuania and <sup>9</sup>Department of Clinical Pharmacology, Sechenov First Moscow State Medical University, Moscow 119435, Russia

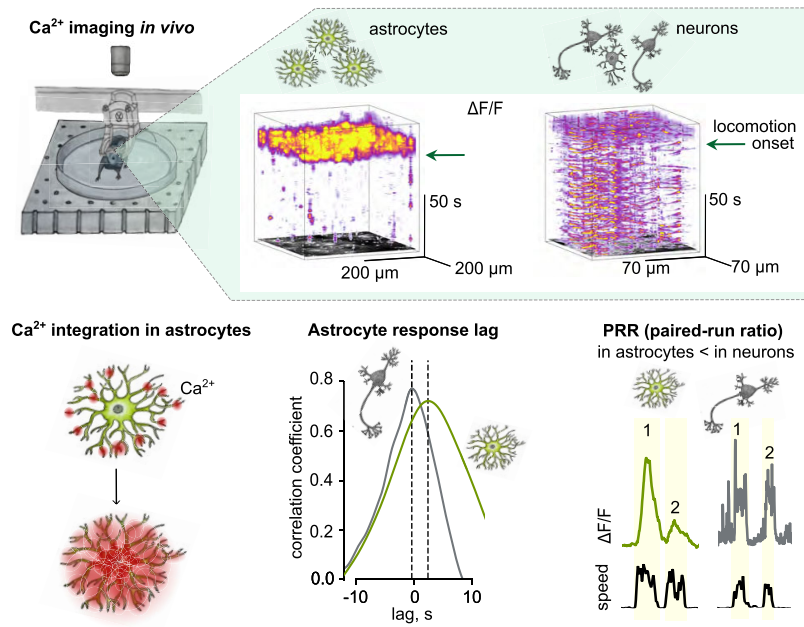
\*Address correspondence to A.V. (e-mail: [Alexej.Verkhatsky@manchester.ac.uk](mailto:Alexej.Verkhatsky@manchester.ac.uk)), A.S. (e-mail: [alexeysemyanov@gmail.com](mailto:alexeysemyanov@gmail.com))

## Abstract

Locomotion triggers a coordinated response of both neurons and astrocytes in the brain. Here we performed calcium ( $\text{Ca}^{2+}$ ) imaging of these two cell types in the somatosensory cortex in head-fixed mice moving on the air-lifted platform.  $\text{Ca}^{2+}$  activity in astrocytes significantly increased during locomotion from a low quiescence level.  $\text{Ca}^{2+}$  signals first appeared in the distal processes and then propagated to astrocytic somata, where it became significantly larger and exhibited oscillatory behaviour. Thus, astrocytic soma operates as both integrator and amplifier of  $\text{Ca}^{2+}$  signal. In neurons,  $\text{Ca}^{2+}$  activity was pronounced in quiescent periods and further increased during locomotion. Neuronal  $\text{Ca}^{2+}$  concentration ( $[\text{Ca}^{2+}]_i$ ) rose almost immediately following the onset of locomotion, whereas astrocytic  $\text{Ca}^{2+}$  signals lagged by several seconds. Such a long lag suggests that astrocytic  $[\text{Ca}^{2+}]_i$  elevations are unlikely to be triggered by the activity of synapses among local neurons.  $\text{Ca}^{2+}$  responses to pairs of consecutive episodes of locomotion did not significantly differ in neurons, while were significantly diminished in response to the second locomotion in astrocytes. Such astrocytic refractoriness may arise from distinct mechanisms underlying  $\text{Ca}^{2+}$  signal generation. In neurons, the bulk of  $\text{Ca}^{2+}$  enters through the  $\text{Ca}^{2+}$  channels in the plasma membrane allowing for steady-level  $\text{Ca}^{2+}$  elevations in repetitive runs. Astrocytic  $\text{Ca}^{2+}$  responses originate from the intracellular stores, the depletion of which affects subsequent  $\text{Ca}^{2+}$  signals. Functionally, neuronal  $\text{Ca}^{2+}$  response reflects sensory input processed by neurons. Astrocytic  $\text{Ca}^{2+}$  dynamics is likely to provide metabolic and homeostatic support within the brain active milieu.

Submitted: 25 March 2023; Revised: 24 April 2023; Accepted: 25 April 2023

© The Author(s) 2023. Published by Oxford University Press on behalf of American Physiological Society. This is an Open Access article distributed under the terms of the Creative Commons Attribution License (<https://creativecommons.org/licenses/by/4.0/>), which permits unrestricted reuse, distribution, and reproduction in any medium, provided the original work is properly cited.



**Key words:** astrocyte; neuron; Ca<sup>2+</sup> signaling; locomotion; in vivo brain imaging; brain active milieu; paired-run ratio

## Introduction

Brain function depends on closely coordinated interactions between different cell types, including neurons, glial cells, cells of the blood vessels, and noncellular elements such as extracellular space and extracellular matrix. This system of brain elements and their interactions is called the brain active milieu.<sup>1,2</sup> The activity of electrically excitable neurons and their synaptic communication have been routinely recorded with electrode-based methods, demonstrating neuronal contribution to major brain functions: locomotion,<sup>3</sup> sensory activity,<sup>4</sup> vision,<sup>5</sup> learning, and memory.<sup>6</sup> Eclectically nonexcitable elements of the brain active milieu, including neuroglia, cannot be fully assessed with electrode-based techniques and require alternative approaches such as real-time optical imaging.

Optical methods allow monitoring of various types of cellular activity in the brain that include ionic signaling,<sup>7–10</sup> metabolic processes,<sup>11,12</sup> cellular morphology, and structure of extracellular space.<sup>13–15</sup> Ca<sup>2+</sup> imaging is the most popular: Multiple genetically encoded sensors were developed to monitor [Ca<sup>2+</sup>]<sub>i</sub> in specific cell types.<sup>16–18</sup>

Two-photon microscopy provides cellular and subcellular resolution for imaging with genetically encoded sensors in vivo.<sup>19–21</sup> However, combining this technique with animal behavior studies is difficult because the animal is kept in a head-fixed restrained condition throughout the experiment. Thus, experiments have been routinely performed on treadmills and air-floating balls that keep animals in a fixed position while allowing a certain type of locomotion.<sup>22,23</sup> These methods can be combined with a virtual reality environment to design various behavioral paradigms.<sup>24,25</sup> However, whether virtual reality faithfully represents the real world as an experimental animal perceives it remains an open question. In addition, a head-restricted animal cannot turn and always runs in a single direction on treadmills. The air-floating ball allows an animal to turn. Yet, the animal's posture differs from that of an animal running on a flat surface: It resembles climbing an object,

with the tail and the hindlimbs positioned below the head and forelimbs.

Using a flat airlifted platform rectifies the limitations of the above systems for 2-photon imaging in awake animals. This technique was used recently to monitor [Ca<sup>2+</sup>]<sub>i</sub> dynamics in neurons and microglia in mice.<sup>26,27</sup> However, the other elements of the brain active milieu have not been systematically studied in this experimental paradigm. Here, we compared the Ca<sup>2+</sup> activity of astrocytes and neurons of mice navigating an airlifted platform.

## Materials and Methods

### Animals

All procedures were performed in accordance with the local guidelines for animal care (The Finnish Act on Animal Experimentation), FELASA ethical recommendations, NIH Guide for the Care and Use of Laboratory Animals, and the animal ethics and welfare committee of Jiaxing University. The C57BL/6 male (N = 6) mice were used in 2-photon imaging experiments. Mice were kept under standard housing conditions with a 12-h light/dark cycle (lights on at 9 AM) with access to water and food ad libitum. Each animal underwent surgery at the age of 12–16 wk, followed by habituation to the experimental setup and imaging sessions. All experiments were carried out during the light period between 10 AM and 5 PM.

### Adeno-associated Virus (AAV) Injection and Cranial Window Implantation

An analgesic (ketoprofen, 2.5 mg/kg) was administered to mice 30 min before the surgery and 24 h postsurgery. Mice were anaesthetized with a mixture of oxygen and isoflurane 1%–1.5% and placed inside the stereotaxic frame apparatus (RWD, Shenzhen, China). To maintain the animal's body

temperature at 37.0°C, a heating pad was used. An eye ointment was applied to the eyes to keep them moist during surgery. The head skin was removed, and a 3-mm craniotomy above the somatosensory cortex was performed using a dental drill (RWD, Shenzhen, China). Throughout the procedure, the skull was kept moist with applications of sterile saline. The stereotaxic injection of AAV5-gfaABC1D-cyto-GCaMP6f (Addgene viral prep #52925-AAV5), titer  $10^{11}$  GC/mL, was performed to get an astrocyte-specific expression of genetically encoded  $\text{Ca}^{2+}$  indicator GCaMP6f in the somatosensory cortex (AP  $-2.3$ , ML  $+0.5$ , DV  $-0.6$ ). To obtain expression in neurons, we used AAV2/9-CaMKII-GCaMP6f, titer  $10^{12}$  GC/mL (VectorBuilder, Guangzhou, China). The total volume of 500 nL was injected via a glass pipette of 5  $\mu\text{L}$  volume (Drummond, USA) using the automatic pump at the rate of 2 nL/s (Ultra Micro Pump III; World Precision Instruments, Sarasota, FL, USA). After each viral injection, the pipette tip was held for 10 min to ensure proper AAV diffusion in the region of interest. Next, 4-mm round cover glass (Warner Instruments, USA) was sealed to the skull with biocompatible adhesive (Vetbond, World Precision Instruments, Sarasota, FL, USA) and universal resin cement RelyX (3M, China). A lightweight stainless steel head plate (model 2, Neurotar, Helsinki, Finland) was mounted on the head with dental acrylic (Super-Bond C&B, Sun Medical, Japan) to restrain a mouse in the experimental setup under the objective of a 2-photon microscope (Femtonics, Budapest, Hungary). Dexamethasone (2 mg/kg) was administered to mice by subcutaneous injection to reduce the surgery-induced inflammation.

### Animal Habituation and Training

Before the imaging sessions, mice were handled and habituated to the experimental setup. Habituation started 3–4 wk after the surgery when the animals fully recovered. Awake mice were head-fixed under a microscope using a Mobile HomeCage device (Neurotar, Helsinki, Finland). Mice heads were secured in the clamping mechanism, and the device was connected to a pressurized air source. Once the carbon fiber cage began to float, animals could move it with their paws. Animals were habituated to head fixation in four to six 2-h training sessions repeated once per day.

### $\text{Ca}^{2+}$ Imaging

After habituation and training, mice were used for  $\text{Ca}^{2+}$  imaging. Multiphoton fluorescence microscope (Femtonics, Budapest, Hungary) with a  $16\times$  NA 0.8 water-immersion objective (CFI75 LWD 16X W, Nikon, Tokyo, Japan) or with a  $20\times$  NA 0.8 water-immersion objective (XLUMPLFLN20XW, Olympus, Tokyo, Japan) was used for  $\text{Ca}^{2+}$  imaging in vivo. Ti:Sapphire laser (Chameleon Ultra, Coherent, USA) with an excitation wavelength of 920 nm was used to excite the fluorescence of GCaMP6f. Fluorescence signal from a brain area of  $600 \times 600$  or  $175 \times 175 \mu\text{m}^2$  ( $512 \times 512$  pixels) was recorded in resonant scanning mode at 30 frames/s. The signal was filtered with a 520/60 nm bandpass filter (Semrock, Rochester, NY, USA) and then detected with a GaAsP photomultiplier (H11706P-40, Hamamatsu, Japan). Simultaneously, autofluorescence was filtered with a 650/100 nm bandpass filter and detected with a second identical photomultiplier. Several imaging sessions of 10 min were carried out for each mouse. In parallel with  $\text{Ca}^{2+}$  imaging, the animal movements on the platform were monitored with locomotion-tracking software

(Neurotar, Helsinki, Finland). All sessions were video recorded in infrared light. The experimental session did not exceed 2 h per mouse.

### Processing $\text{Ca}^{2+}$ Imaging Data

A few procedures and basic estimated parameters were the same for astrocytic and neuronal  $\text{Ca}^{2+}$  data. At the same time, some extracted characteristics differed to match the disparities in the responses of the 2 cell types. Preprocessing steps were identical for both astrocytic and neuronal data. Most of the image processing was done using routines from Image-funcut, uCats, and other software developed in the group using the common scientific Python library stack (SciPy, Scikit-learn, Scikit-image).<sup>28,29</sup>

### Preprocessing: Temporal Binning, Motion Correction, and Denoising

The raw imaging data recorded at 30 Hz were binned along a time dimension by summing intensity values in nonoverlapping batches of 5 frames before further processing to increase the signal-to-noise ratio. Next, rigid-body motion correction was applied using an autofluorescence signal recorded in the red channel as a morphology marker. For a more stable shift estimation, the autofluorescence signal was adaptively denoised by approximating each frame by the first 50 spatial principal components, smoothed by a Gaussian filter with  $\sigma = 1$  pixel. The spatial displacements estimated for the autofluorescence channel have then been applied to the green channel containing GCaMP6f fluorescence.

After shift correction, the data were further denoised using the algorithm developed in the lab. In brief, the data were Anscombe transformed to stabilize variance, and then the recording was divided into overlapping spatial windows (patches), where the data are approximated by truncated SVD with a smoothing filter applied to the spatial components, which is then followed by inverse SVD and Anscombe transforms, averaging the approximations in the overlapping parts of the patches.

### Calculation of $\Delta F/F$ and Active Area

Slowly varying fluorescent baseline level  $F_0$  was determined as a lower envelope running through local minima of the fluorescence signal in each pixel, smoothed by a Gaussian filter with  $\sigma = 15$  s. The resulting baselines were negatively biased, and to correct this bias, the baseline signals in each pixel were then shifted by a constant parameter minimizing the absolute value of the mode of the residuals after baseline subtraction, assuming that most frequent fluctuations are small and are due to noise, while true  $\text{Ca}^{2+}$  events are sparse. Further analysis is done on relative fluorescence changes  $\Delta F/F = (F - F_0)/F_0 \times 100\%$ . An arbitrarily chosen threshold of 15% increase over the baseline ( $\Delta F/F \geq 15\%$ ) was selected as it provided the most visually informative results. Clusters of suprathreshold pixels larger than 16 pixels within a frame were marked as an “active segment” if they produced overlapping structures in at least 3 consecutive frames. The fractional area of such active segments in each frame normalized to the total stained area within the field of view was named “active area” and used to characterize the collective  $\text{Ca}^{2+}$  activity.

## Analysis Specific to Astrocytes

Individual astrocytic domains were visually identified and manually traced. Inside the domain territory, the soma was likewise outlined. The rest of the domain was called processes.  $\Delta F/F$  timecourses were plotted for both processes and soma. Then, the timecourses were normalized to their peak values. The latency between soma and processes was estimated as the difference between the times when  $\Delta F/F$  reached 15% of the maximal value. The prominence of  $\Delta F/F$  oscillations was estimated by averaging wavelet power in the interval when the signal was above 15% of the peak value in the frequency range 0.1–0.3 Hz (continuous wavelet transform, Morlet wavelet).

## Analysis Specific to Neurons

Because neuronal  $\text{Ca}^{2+}$  data displayed a high spatially localized spontaneous activity, we employed a slightly modified constrained non-negative matrix decomposition (CNMF) approach to visualize this activity during locomotion.<sup>30</sup> CNMF is initially optimized for extracting  $\text{Ca}^{2+}$  dynamics from cell bodies, but lifting temporal dynamics and spatial localization constraints can allow for the segmentation of sparse components. The algorithm was applied in overlapping  $100 \times 100$  patches with 12 components per patch to solve for. A second run of the algorithm on the entire frame with the patch-based components as the initial condition was then applied to refine the segmentation. The resulting spatial components could still contain irregular low-amplitude shapes, which were clipped by using Li's auto threshold algorithm on nonzero pixels in each component.<sup>31</sup> The resulting solution produced many spatial segments with similar dynamics, further merged by clustering their corresponding dynamics (agglomerative clustering with Ward linkage) to produce 12 final spatial regions of interest (ROIs).

## Statistical Analysis

Data are presented as median [25th–75th percentiles]. The sample number ( $n$ ) indicates the number of recordings, periods of locomotion or quiescence, or cells and is specified for each experiment. Astrocytic  $\text{Ca}^{2+}$  activity was recorded in 2 mice and neuronal in 4 mice. Statistical analysis was conducted using Python. For comparison of astrocytic and neuronal  $\text{Ca}^{2+}$  activity ( $\Delta F/F$  and active area) during the periods of quiescence and locomotion, the nonparametric Mann–Whitney  $U$ -test was used. For other comparisons, linear mixed-effects models were applied.<sup>32</sup> The experimenters were not blinded to the experimental conditions, and no randomization was performed. All statistical details of the experiments are provided in the main text and figure legends.  $P < .05$  was considered statistically significant.

## Results

### $\text{Ca}^{2+}$ Activity in Cortical Astrocytes Is Linked to Locomotion but Not Location

The somatosensory cortex area of mice containing projections of the left forelimb was injected with an AAV for expression of genetically encoded  $\text{Ca}^{2+}$  sensor GCaMP6f under either astrocytic (AAV5-gfaABC1D-cyto-GCaMP6f) or neuronal (AAV2/9-CamKII-GCaMP6f) promoters (Figure 1A). The cranial

glass window was implanted above the site of injection. A lightweight stainless steel head plate was glued above the window. After recovery from the surgery, the animals were left for 3–4 wk in individual cages for GCaMP6f expression. After handling the animals and their habituation to the air-lifted platform,  $\text{Ca}^{2+}$  imaging experiments were performed (Video S1).

First, the imaging was done on astrocytes expressing GCaMP6f in cortical layer 1 (Figure 1B; Video S2). The animal locomotion episodes alternated with quiescence periods (Figure 1C and D). During quiescent periods,  $\text{Ca}^{2+}$  activity appeared as small, scattered events.<sup>10</sup> Jointly, these events covered only a tiny frame area (mean active area per period of quiescence: 1.0 [0.8–1.7]% of frame;  $n = 21$ ) and had low  $\Delta F/F$  (mean  $\Delta F/F$  per period of quiescence: 1.4 [1.0–1.6]%;  $n = 21$ ). Consistent with previous reports, the locomotion was accompanied by a rise in astrocytic  $[\text{Ca}^{2+}]_i$ .<sup>20,33,34</sup> We observed an increase in both the active area (mean active area per episode of locomotion: 20.2 [10.7–36.1]% of frame;  $n = 29$ ;  $P < .001$ , mixed-effects model) and  $\Delta F/F$  (mean  $\Delta F/F$  per episode of locomotion: 9.9 [6.3–19.2]%;  $n = 29$ ;  $P < .001$ , mixed-effects model). Sometimes, the animal ran several times with short intervals of quiescence. Astrocytic  $[\text{Ca}^{2+}]_i$  increased during each running episode, but this increase became smaller in subsequent episodes.

Astrocytic  $\text{Ca}^{2+}$  imaging was combined with animal tracking (Figure 1E). The mouse ran for several seconds in each episode and moved around the entire territory of the platform during the experiment. However, the animal preferred to rest (quiescence period) at the platform's periphery.  $\text{Ca}^{2+}$  activity followed the locomotion pattern without an obvious link to the animal's location.

## Integrative Function of Astrocytes

Spontaneous  $\text{Ca}^{2+}$  events are primarily localized to distal astrocytic processes.<sup>35,36</sup> We observed that during locomotion,  $[\text{Ca}^{2+}]_i$  increased in the entire astrocytic domain, including soma. This observation prompts a question of whether  $\text{Ca}^{2+}$  activity initiated in soma subsequently diverges to astrocytic processes or  $[\text{Ca}^{2+}]_i$  rises in distal processes propagate toward the soma. We performed a wide line-scan across the entire astrocytic domain and then analyzed  $[\text{Ca}^{2+}]_i$  changes in soma and processes (Figure 2A). During the mouse running episode  $[\text{Ca}^{2+}]_i$  elevations started in distal parts of the astrocytic domain and then propagated to the soma (Figure 2B). This phenomenon was also observed in the consecutive frames showing  $\Delta F/F$  over cell morphology image (Figure 2C). Notably,  $\text{Ca}^{2+}$  response also first faded in the soma at the end of the running episode.

Next, we compared the timecourses of  $\Delta F/F$  sampled from the soma and the processes (Figure 2D and E). First, maximal  $\Delta F/F$  was significantly larger in the soma (processes: 170.3 [102.8–229.7]%,  $n = 53$ ; soma: 465.0 [245.1–595.3]%;  $n = 53$ ;  $P < .001$ , mixed-effects model; Figure 2F). Second, we observed that periodic  $[\text{Ca}^{2+}]_i$  oscillations, which were more pronounced in soma than in astrocytic processes (wavelet power; processes: 0.06 [0.03–0.10] a.u.,  $n = 53$ ; soma: 0.21 [0.10–0.42] a.u.;  $n = 53$ ;  $P < .001$ , mixed-effects model; Figure 2G and H). Finally, we measured the latency between  $\Delta F/F$  increases in the soma and the processes (4.7 [2.3–8.9] s,  $n = 53$ ; Figure 2I). Because the latency varied in a wide range, we tested if this variability can be explained by the variability in astrocyte domain size. However, we did not find a significant correlation between the latency and the astrocyte maximum Feret diameter ( $R^2 = 0.055$ ,  $P = .09$ , linear regression,  $n = 53$ ; Figure 2J).



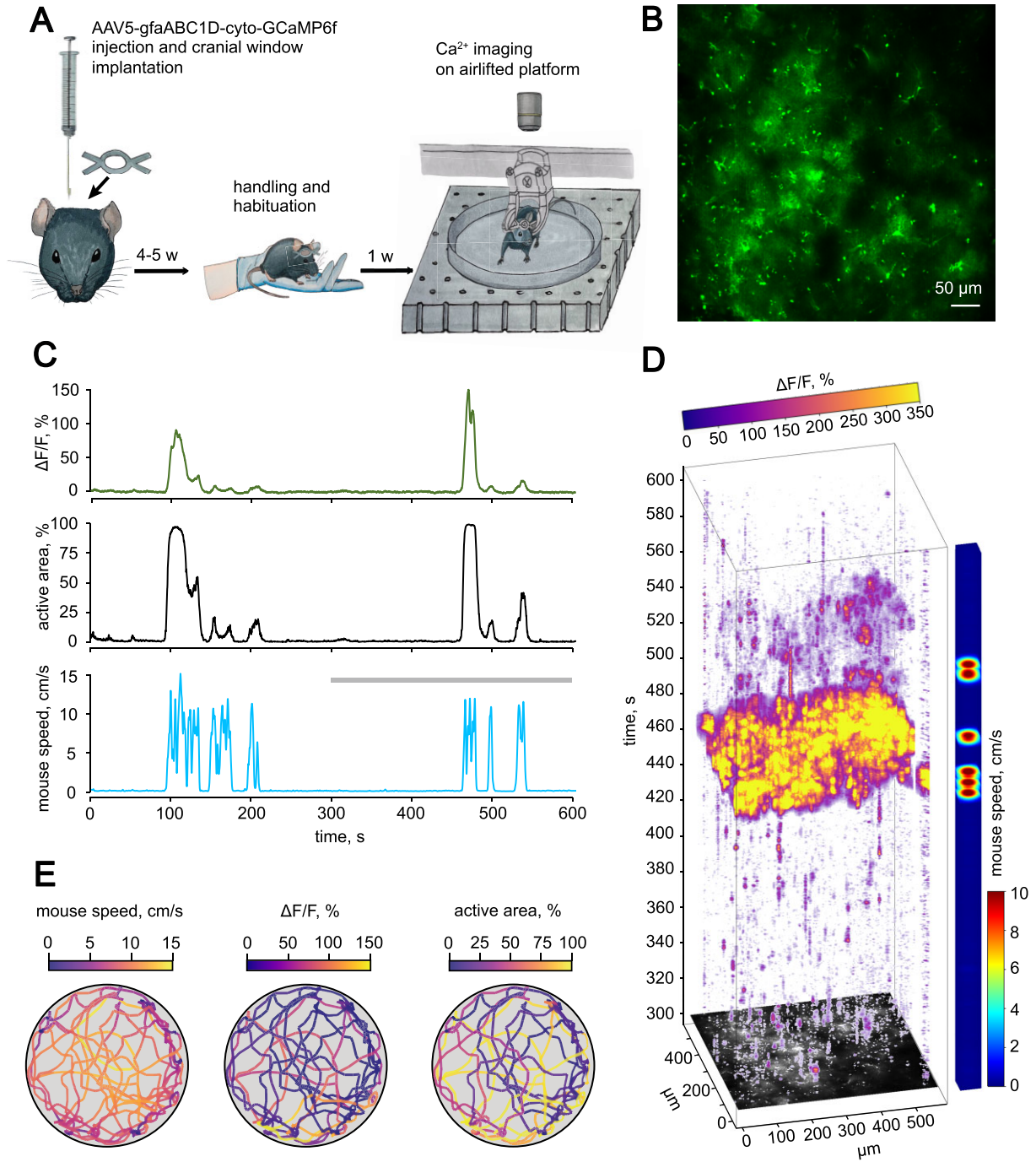


**Figure 1.** Properties of Ca<sup>2+</sup> activity in cortical astrocytes during locomotion. (A) Experimental design: AAV5-gfaABC1D-cyto-GCaMP6f was injected into the somatosensory cortex of a C57Bl/6 mouse, followed by chronic cranial window implantation. After 3–4 wk of GCaMP6f expression, mice were handled and habituated to the experimental setup. Ten-minute Ca<sup>2+</sup> imaging sessions combined with animal tracking were performed after the training procedure. (B) The fluorescence signal from cortical astrocytes expressing GCaMP6f in an awake mouse. (C) The timecourses of  $\Delta F/F$  (top), the active area (middle), and the mouse speed (bottom). The gray line indicates the part of the recording used for the reconstruction shown in panel (D). (D) The 3-dimensional reconstruction (x–y time) of  $\Delta F/F$  values showing the distribution of astrocytic Ca<sup>2+</sup> activity over the imaged region in time. The colored bar on the right-hand side encodes the speed of the animal. (E) The animal track recorded for 600 s color-coded with the mouse speed (left),  $\Delta F/F$  (middle), and the active area (right).

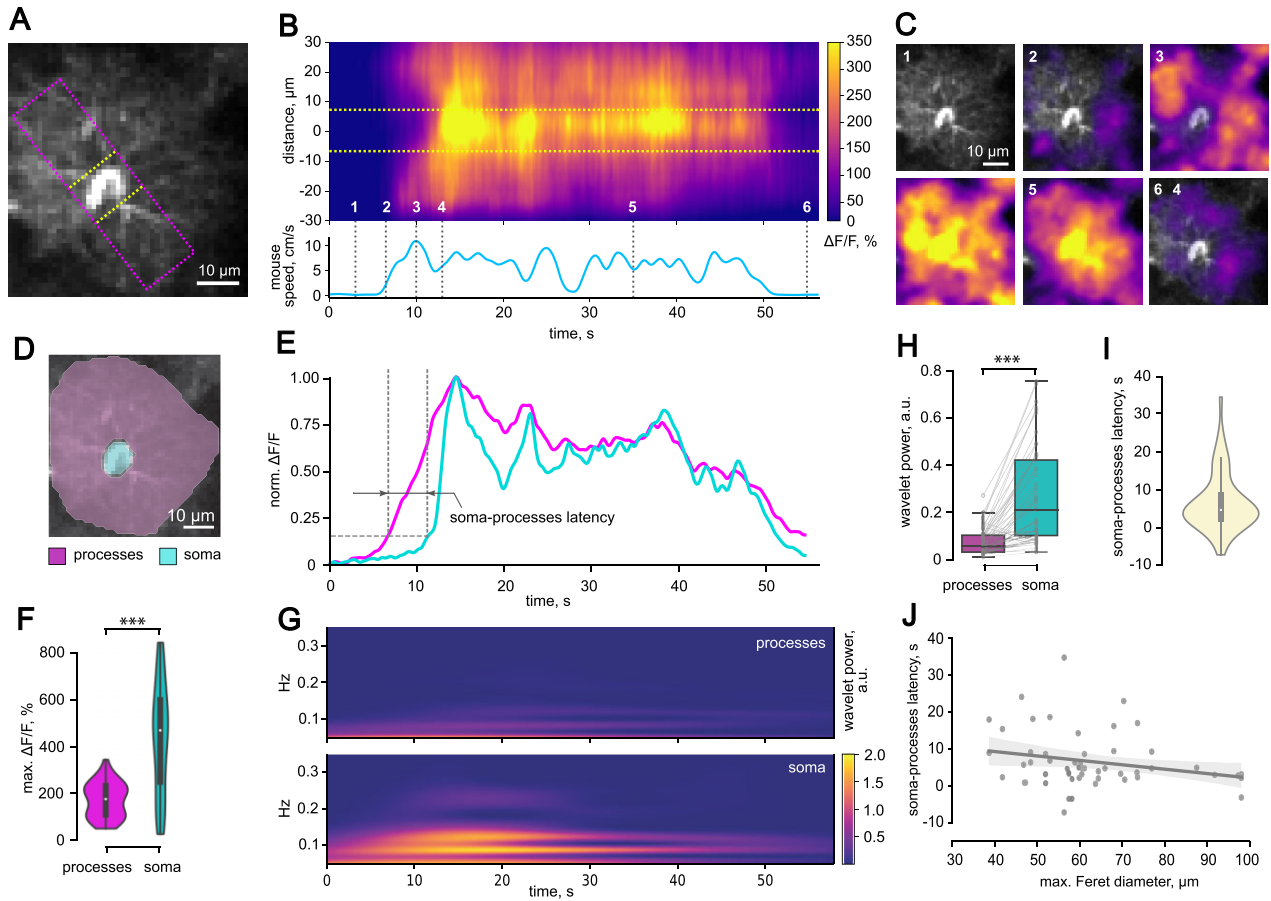


**Figure 2.** Locomotion-induced  $\text{Ca}^{2+}$  activity in a single astrocyte. (A) An astrocyte image with the position of a wide line-scan (pink rectangle). Yellow dotted lines indicate the soma. (B) (Top) The fluorescence line-scan (x-t) image showing  $\text{Ca}^{2+}$  response to locomotion in the astrocytic processes and the soma. The distance was calculated from the center of the soma (0  $\mu\text{m}$ ). The yellow dotted lines mark the width of the soma. (Bottom) The timecourse of mouse speed during the locomotion episode corresponding to the above line-scan. (C) The spatial distribution of  $\text{Ca}^{2+}$  activity ( $\Delta F/F$ ) for the time points indicated in (B) by the dotted lines. (D) An astrocyte segmented to the soma and the processes. (E) The timecourses of  $\text{Ca}^{2+}$  activity ( $\Delta F/F$ ) normalized to the maximal  $\Delta F/F$  in the astrocytic soma and processes during the episode of locomotion shown at (B). Soma-processes latency was calculated between the points corresponding to 15% of the maximal  $\Delta F/F$  (dotted lines and arrows). (F) Summary data of maximal  $\Delta F/F$  in the processes and the somata (\*\*\* $P < .001$ , mixed-effects model,  $n = 53$  cells). (G) The wavelet spectrograms of the fluorescent signals shown in (E). (H) Average wavelet power (a.u.) taken over interval when  $\Delta F/F$  in the astrocytic processes (top) and soma (bottom) was above 15% of the peak and within 0.1–0.3 Hz frequency range (\*\*\* $P < .001$ , mixed-effects model,  $n = 53$  cells). (I) The distribution of soma-processes latencies of  $\text{Ca}^{2+}$  responses. (J) The relationship between soma-processes latency of  $\text{Ca}^{2+}$  responses and astrocyte size expressed as maximum Feret diameter (Regression analysis:  $R^2 = 0.055$ ,  $P = .09$ , linear regression,  $n = 53$  cells).

These results suggest that  $\text{Ca}^{2+}$  signals start in astrocytic processes and converge into soma during animal locomotion. Astrocytic soma integrates the  $\text{Ca}^{2+}$  signal, amplifies it, and generates  $\text{Ca}^{2+}$  oscillations.

### Neuronal $\text{Ca}^{2+}$ Response to Locomotion

Neuronal  $\text{Ca}^{2+}$  activity was recorded in cortical layer 1 (Figure 3A). In this layer, we rarely saw somata of the neurons but observed multiple processes. Some of these processes can be visually identified as dendrites with spines, and others cannot be classified into any specific type (dendrites or axons). Many neuronal processes exhibited high  $\text{Ca}^{2+}$  activity during quiescent periods (Figure 3B and C; Video S3). Thus, unlike astrocytes, the neurons were active during locomotion and quiescent periods.

During quiescent periods, the mean active area was 6.0 [4.4–9.4]% of the frame ( $n = 37$ ), and the mean  $\Delta F/F$  per period of quiescence was 3.1 [2.7–4.2]% ( $n = 37$ ). Locomotion was

accompanied by a rise in neuronal  $[\text{Ca}^{2+}]_i$  (mean active area per episode of locomotion: 53.4 [43.8–62.2]%,  $n = 29$ ;  $P < .001$ , mixed-effects model; mean  $\Delta F/F$  per episode of locomotion: 19.5 [16.5–26.8]%,  $n = 29$ ;  $P < .001$ , mixed-effects model).

To identify how different neuronal compartments contribute to  $\text{Ca}^{2+}$  dynamics during quiescent periods and locomotion, we applied a constrained non-negative matrix factorization (CNMF) approach implemented in CalmAn, open-source software for  $\text{Ca}^{2+}$  imaging analysis.<sup>37</sup> With CNMF followed by clustering, we identified neuronal structures activated synchronously within individual recordings (Figure 3D). These structures represented separate neuronal processes. We cannot confidently conclude whether these processes belong to the same neuron; thus, we considered them activity units. We analyzed each activity unit by plotting the corresponding  $[\text{Ca}^{2+}]_i$  timecourses (Figure 3E). Such analysis revealed 2 types of units, which had either high activity or low activity during quiescent periods. In the low activity, units  $[\text{Ca}^{2+}]_i$  increased during locomotion. In the high activity, units  $[\text{Ca}^{2+}]_i$  did not

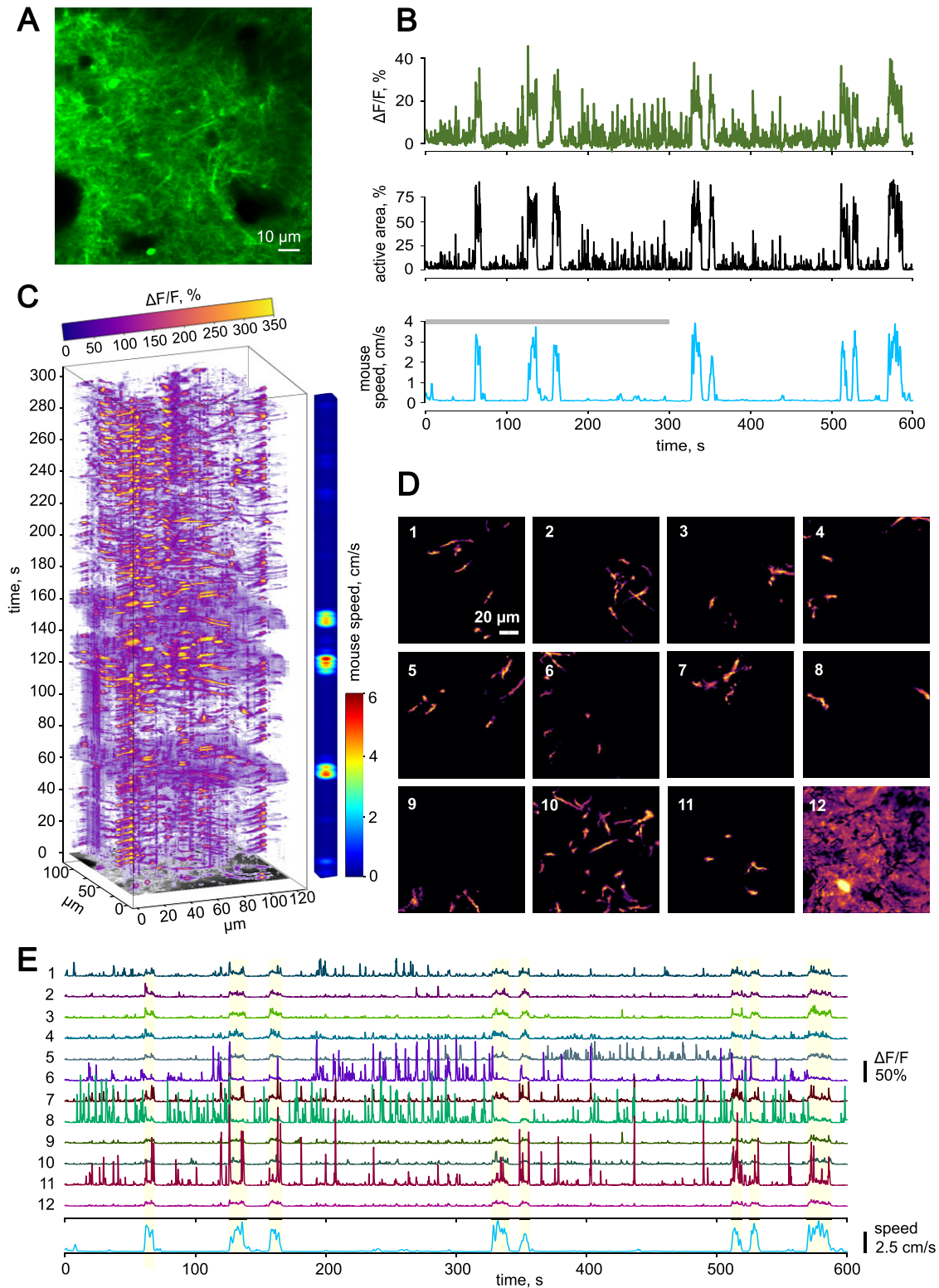


**Figure 3.** Properties of  $\text{Ca}^{2+}$  activity in cortical neurons during locomotion. (A) The fluorescence signal from cortical neurons expressing GCaMP6f in an awake mouse. (B) The timecourses of  $\Delta F/F$  (top), the active area (middle), and the mouse speed (bottom). The gray line indicates the part of the recording used for the reconstruction shown in (C). (C) The 3-dimensional reconstruction (x-y time) of  $\Delta F/F$  values showing the distribution of neuronal  $\text{Ca}^{2+}$  activity over the imaged region in time. The colored bar on the right side encodes the speed of the animal. (D) ROIs or units of synchronous neuronal  $\text{Ca}^{2+}$  activity segmented with CNMF-based approach within the recording presented at (B) and (C). (E) The timecourses of  $\text{Ca}^{2+}$  activity ( $\Delta F/F$ ) in individual ROIs (activity units) shown and numbered at (D). The blue timecourse at the bottom is animal speed. Light yellow-shaded regions represent episodes of locomotion.



increase and in some cases decreased. Also, we noticed that the  $[Ca^{2+}]_i$  increased during locomotion in the regions where we could not unequivocally identify neuronal structures. These regions may correspond to the out-of-focus or dim structures.

### Dissociation Between Neuronal and Astrocytic $Ca^{2+}$ Response to Locomotion

Next, we compared the parameters of  $Ca^{2+}$  responses to locomotion between astrocytes and neurons. First, we measured mean  $\Delta F/F$  during the quiescent period (Q) and locomotion (L). The Q/L ratio of  $\Delta F/F$  was significantly higher in neurons than in astrocytes (in neurons: 0.18 [0.14–0.20],  $n = 8$ ; in astrocytes: 0.067 [0.044–0.092],  $n = 7$ ;  $P < .001$ , Mann–Whitney  $U$ -test; Figure 4A and B). The Q/L ratio calculated for the active area was also significantly higher in neurons (in neurons: 0.13 [0.11–0.16],  $n = 8$ ; in astrocytes: 0.039 [0.0036–0.061],  $n = 7$ ;  $P = .001$ , Mann–Whitney  $U$ -test; Figure 4C). These results reflect higher  $Ca^{2+}$  activity in neurons during quiescent periods as compared to astrocytes.

Second, we asked when  $Ca^{2+}$  response in neurons and astrocytes develops relative to locomotion. We performed cross-correlations of locomotion speed and  $[Ca^{2+}]_i$  elevations ( $\Delta F/F$ ) in neurons and astrocytes. The cross-correlations yielded reasonably high peak coefficients in both cell types (in neurons: 0.72 [0.46–0.79],  $n = 8$ ; in astrocytes: 0.63 [0.59–0.67],  $n = 8$ ;  $P = .87$ , mixed-effects model; Figure 4D and E). In neurons, the time of the peak was around 0, suggesting that locomotion and  $[Ca^{2+}]_i$  elevation coincided (–0.16 [–0.67–0.08] s,  $n = 8$ ). In astrocytes, the peak had a lag of several seconds (2.5 [1.6–8.3],  $n = 8$ ;  $P < .001$ , mixed-effects model; Figure 4F). This result indicates that  $Ca^{2+}$  response in astrocytes develops several seconds after the beginning of the locomotion episode and neuronal  $Ca^{2+}$  response.

Finally, we compared neuronal and astrocytic responses to 2 consecutive episodes of locomotion. We selected pairs of closely timed running episodes with less than 30 s intervals. Then, we calculated the paired-run ratio (PRR) as the ratio between the peaks of second and first  $Ca^{2+}$  responses ( $\Delta F/F$  or active area) corresponding to 2 locomotion episodes (Figure 4G). The PRR of  $\Delta F/F$  in neurons was close to 1 (0.96 [0.80–1.11],  $n = 7$ ; Figure 4H) suggesting that neurons reliably respond to each locomotion episode. Conversely, PRR of  $\Delta F/F$  in astrocytes was significantly lower than in neurons (0.32 [0.267–0.67],  $n = 14$ ;  $P = .002$ , mixed-effects model) suggesting a decline in astrocytic response. Similar results were obtained for PRR of active area (in neurons 0.93 [0.80–1.14],  $n = 7$ ; in astrocytes 0.33 [0.18–0.83],  $n = 14$ ;  $P = .014$ , mixed-effects model; Figure 4I). These findings demonstrate that neuronal  $Ca^{2+}$  activity reliably increases with every locomotion episode. In contrast, astrocytic  $Ca^{2+}$  signal has refractoriness that prevents  $Ca^{2+}$  response from developing during closely timed locomotion episodes.

## Discussion

### The Distinct Timecourses of Neuronal and Astrocytic $Ca^{2+}$ Response to Locomotion

Cortical neurons receive sensory input from thalamic nuclei. During locomotion, neuronal firing triggers  $Ca^{2+}$  entry through voltage-gated  $Ca^{2+}$  channels. We observed that overall neuronal

$Ca^{2+}$  activity in the somatosensory cortex increased during animal locomotion. However, neurons remained active in quiescent periods between episodes of locomotion. In some neuronal units, activity during quiescence was higher than that during locomotion.

Local  $[Ca^{2+}]_i$  elevations in astrocytic leaflets can be mediated by  $Ca^{2+}$  entry through the plasma membrane (through ionotropic receptors or reversed  $Na^+/Ca^{2+}$  exchanger), whereas large  $Ca^{2+}$  transients in soma and branches are mediated by  $Ca^{2+}$  release from endogenous stores—endoplasmic reticulum and mitochondria.<sup>38–40</sup> During animal quiescence, astrocytes generated small, scattered  $Ca^{2+}$  events. These events can be either spontaneous or triggered by local synaptic activity. During locomotion, astrocytic  $Ca^{2+}$  activity substantially increased. Relative to  $Ca^{2+}$  activity during the quiescent period, this increase was significantly larger in astrocytes than in neurons. Moreover, astrocytic  $[Ca^{2+}]_i$  elevation was delayed for several seconds after the beginning of the locomotion episode and neuronal  $[Ca^{2+}]_i$  elevation. These findings suggest that the activity of the local neuronal network may not trigger the astrocytic  $Ca^{2+}$  signal. Most likely, astrocytic response originates from modulatory subcortical projections, such as noradrenergic input from the locus coeruleus targeting adrenergic receptors abundantly expressed in mature astrocytes.<sup>41–43</sup> Delayed astrocytic  $Ca^{2+}$  response also raises a question of its physiological relevance. This delay suggests that astrocytes do not respond to sensory signals in real time, hence are involved in the real-time processing of sensory information. On the other hand, astrocytic  $Ca^{2+}$  activity may be involved in modulation of synaptic plasticity,<sup>44</sup> regulation of vascular tone,<sup>45</sup> and metabolic activation of astrocytes<sup>46</sup> that occur with a delay. For example, synaptic plasticity and memory consolidation may happen after sensory information is processed, filtered, and compared to previous memories in the brain. The same applies to vasodilatation and metabolic activation of astrocytes, which can represent a systemic response to the increased energy demand of the brain following robust neuronal activity during locomotion.<sup>47</sup>

### A Refractory Period of $Ca^{2+}$ Activity in Astrocytes

Another example of dissociation between  $Ca^{2+}$  activity in the local neuronal network and astrocytes is highlighted by distinct changes in the PRR. When an animal ran twice with a short interval (<30 s), the neuronal network reliably responded to each locomotion episode. Astrocytes responded with a large  $Ca^{2+}$  transient only to the first run. The response to the second run was significantly diminished. Most likely, it is related to the mechanisms of  $Ca^{2+}$  signal generation in these 2 cell types. In neurons, the bulk of  $Ca^{2+}$  enters through ligand- or voltage-gated channels of the plasma membrane.<sup>48,49</sup> Because the transmembrane  $Ca^{2+}$  gradient is quickly restored, neurons are ready to respond to the second run. Global astrocytic  $Ca^{2+}$  transients depend on  $Ca^{2+}$  release through inositol 1,4,5-trisphosphate receptors (InsP<sub>3</sub>R) from the endoplasmic reticulum, which, upon strong stimulation, gets depleted, while InsP<sub>3</sub>R become inactivated.<sup>39,40,50</sup> It takes substantially more time to restore the ability to generate  $Ca^{2+}$  signals for astrocytes than for neurons. What is the physiological relevance of such a refractory period? Astrocytic  $Ca^{2+}$  stimulates oxidative phosphorylation.<sup>51</sup> However, due to the sparse distribution of cytochromes in the astrocytic electron transport chain, there is also a high probability of reactive oxygen species (ROS) generation in response to  $[Ca^{2+}]_i$  elevation in astrocytes.<sup>52,53</sup> In moderate quantities,



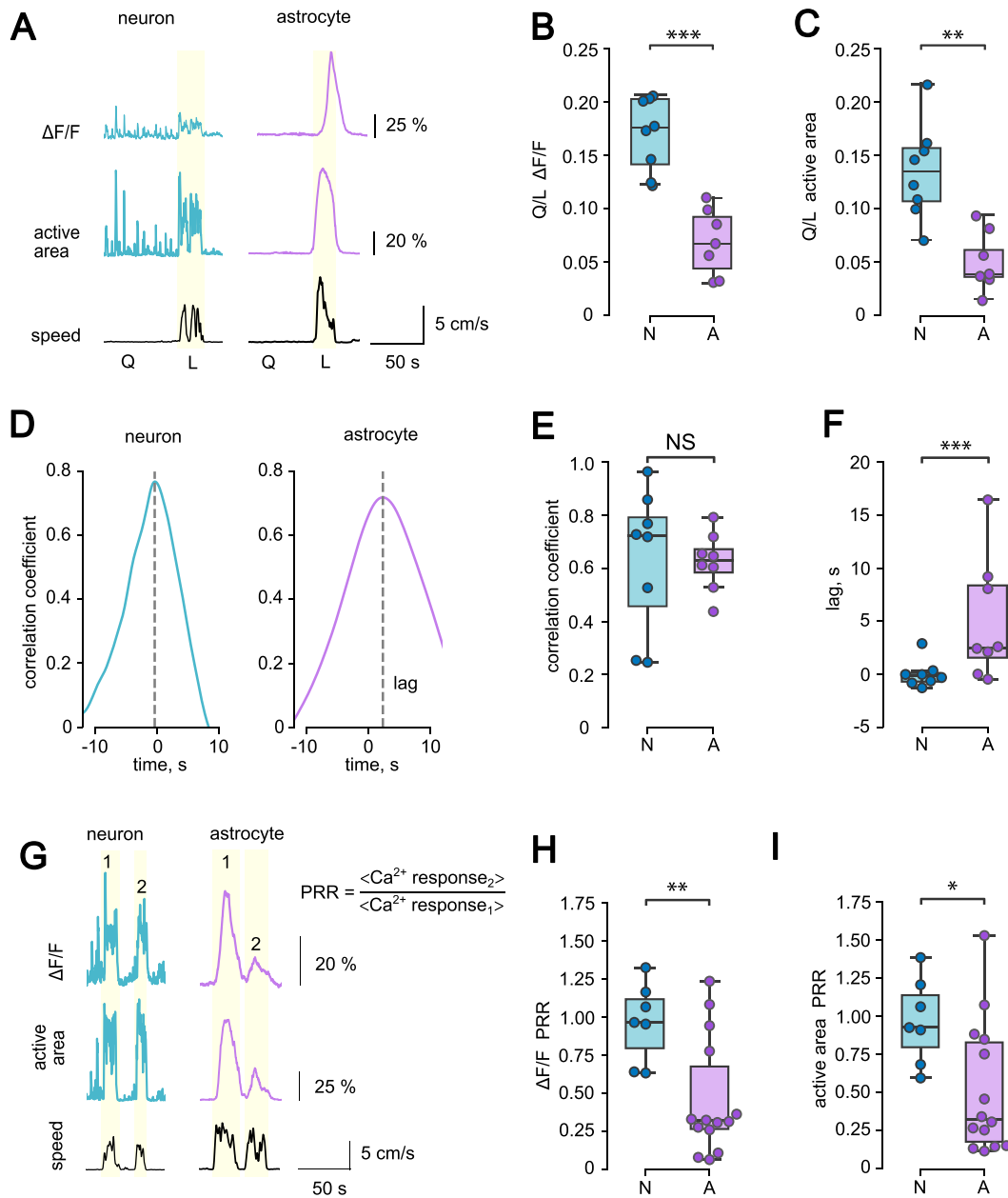


**Figure 4.** Comparison of locomotion-induced  $Ca^{2+}$  responses in neurons and astrocytes. (A) The timecourses demonstrating changes in  $\Delta F/F$  (top) and active area (middle) of neuronal (left) and astrocytic (right)  $Ca^{2+}$  activity during the periods of quiescence (Q) and locomotion (L). (Bottom) The timecourse of animal speed. (B and C) Q/L ratio, calculated for  $Ca^{2+}$  activity in cortical neurons (“N,”  $n = 8$  recordings) and astrocytes (“A,”  $n = 7$  recordings;  $***P < .001$  and  $**P = .001$  for  $\Delta F/F$  (B) and active area (C), respectively, Mann-Whitney  $U$ -test). (D) Cross-correlation graphs between  $\Delta F/F$  and animal speed for neurons (left) and astrocytes (right) during an episode of locomotion. (E) Peak correlation coefficients for neurons (“N,”  $n = 8$  recordings) and astrocytes (“A,”  $n = 7$  recordings;  $P = .87$ , mixed-effects model) for the analysis presented at (D). (F) Lag of cross-correlation peak in neurons (“N,”  $n = 8$  recordings) and astrocytes (“A,”  $n = 7$  recordings;  $***P < .001$ , mixed-effects model). (G) The timecourses demonstrating changes in  $\Delta F/F$  (top) and active area (middle) of neuronal (left) and astrocytic (right)  $Ca^{2+}$  activity during pairs of locomotion episodes. (Bottom) The timecourse of animal speed. The formula is for PRR calculation where  $\langle Ca^{2+} \text{ response}_1 \rangle$  is the mean  $Ca^{2+}$  response to the first locomotion in 1 recording;  $\langle Ca^{2+} \text{ response}_2 \rangle$  is the same for the second locomotion. (H and I) PRRs for  $\Delta F/F$  ( $**P = .002$ , mixed-effects model) and active area ( $*P = .014$ , mixed-effects model) in neurons (“N,”  $n = 7$  paired runs) and astrocytes (“A,”  $n = 14$  paired runs).

ROS play a signaling role and promote synaptic plasticity in the brain.<sup>54</sup> In high quantities, they cause oxidative stress and cell damage. Therefore, the astrocytic refractory period may preserve ROS's beneficial effects while preventing cell damage.

### Integrative Function of Astrocytes

At the subcellular level,  $[Ca^{2+}]_i$  did not increase simultaneously in the entire astrocytic morphological domain during locomotion.  $[Ca^{2+}]_i$  elevation started in the distal processes

and then propagated into the soma. This finding is consistent with a higher probability for  $\text{Ca}^{2+}$  activity generation in distal astrocytic processes.<sup>35,55</sup> This phenomenon may be explained by the specific localization of synapses near distal astrocytic processes. However, a recent report demonstrated a relatively even distribution of synapses near distal processes and astrocytic soma.<sup>56</sup> An alternative explanation is that distal astrocytic processes have a higher surface-to-volume ratio (SVR).<sup>36</sup> High SVR increases the amplitudes of  $[\text{Ca}^{2+}]_i$  elevations induced by  $\text{Ca}^{2+}$  entry through the plasma membrane and consequently increases the probability of  $\text{Ca}^{2+}$ -dependent  $\text{Ca}^{2+}$  release from endogenous stores.

Our observations also suggest that astrocytic soma operates as an integrator of  $\text{Ca}^{2+}$  activity starting in the processes.  $\text{Ca}^{2+}$  signal integration in astrocytic soma is reminiscent of the integration of membrane voltage changes from dendritic inputs by soma in neurons.<sup>57</sup> However, in the case of neurons, somatic integration is translated into a pattern of action potentials. What is the functional relevance of  $\text{Ca}^{2+}$  activity integration in astrocytes? One possibility is an amplification of the  $\text{Ca}^{2+}$  signals. The  $\text{Ca}^{2+}$  response in soma was several fold higher than that in the processes. Different levels of  $[\text{Ca}^{2+}]_i$  regulate distinct molecular pathways.<sup>58</sup> Thus,  $\text{Ca}^{2+}$  amplification may target specific cellular functions. For example, somatic  $[\text{Ca}^{2+}]_i$  elevation can boost ATP production by promoting the activity of the tricarboxylic acid cycle enzymes, the proteins of the electron transport chain, and the ATP synthase.<sup>59,60</sup> Such enhanced metabolic response of astrocyte can be the physiological outcome of  $\text{Ca}^{2+}$  integration, homologues to, and yet distinct from, synaptic integration and action potential generation in neurons.

### $\text{Ca}^{2+}$ Oscillations in Astrocytic Soma

In addition,  $\text{Ca}^{2+}$  integration in astrocytic soma triggers  $[\text{Ca}^{2+}]_i$  oscillations.  $[\text{Ca}^{2+}]_i$  oscillations in astrocytes were routinely recorded in primary cultures and in slices in response to pharmacological stimulation.<sup>61–64</sup> Mathematical models of astrocytic  $[\text{Ca}^{2+}]_i$  dynamics also predict oscillatory activity due to positive and negative feedbacks.<sup>65,66</sup> Although astrocytes, in principle, should possess mechanisms for  $[\text{Ca}^{2+}]_i$  oscillations, oscillatory behavior was not reported in vivo. A possible reason is that  $\text{Ca}^{2+}$  activity in astrocytes in vivo is defined by inputs from many elements of the brain active milieu (local neuronal network, neuromodulatory projections, blood vessels, etc.), which drive the sequence of astrocytic  $\text{Ca}^{2+}$  events. However, astrocyte oscillatory mechanisms can re-emerge during somatic  $[\text{Ca}^{2+}]_i$  elevations. These oscillations originate specifically in the soma and fade away when propagating toward the astrocytic periphery.  $[\text{Ca}^{2+}]_i$  oscillations require  $[\text{Ca}^{2+}]_i$  to exceed a certain threshold. Large  $[\text{Ca}^{2+}]_i$  elevations and well-expressed  $\text{Ca}^{2+}$  stores in the soma provide optimal conditions for  $[\text{Ca}^{2+}]_i$  oscillations.<sup>65</sup> Possibly, the information is encoded in the frequency of  $[\text{Ca}^{2+}]_i$  oscillations that depends on the strength of the external signal and intrinsic properties of an individual astrocyte. The oscillatory  $\text{Ca}^{2+}$  signal is decoded by the enzymes containing  $\text{Ca}^{2+}$  binding motifs with a distinct affinity that can regulate their phosphorylation and activate specific cellular programs.<sup>67</sup>

### Conclusion

We demonstrate that  $\text{Ca}^{2+}$  dynamics in astrocytes does not follow neuronal  $\text{Ca}^{2+}$  activity that accompanies locomotion, indicating that astrocytic  $[\text{Ca}^{2+}]_i$  is controlled by pathways distinct from sensory inputs that activate neuronal networks. While

neuronal  $[\text{Ca}^{2+}]_i$  faithfully follows episodes of animal locomotion, astrocytic  $\text{Ca}^{2+}$  signals develop on a different timescale, compatible with distinct roles astrocytes play in sustaining nervous tissue and supporting neuronal information processing and storage.

### Acknowledgements

The authors thank Tamás Kopcsányi for providing his help with surgical training and technical assistance.

### Supplementary material

Supplementary material is available at the APS Function online.

### Funding

The work was supported by the Russian Science Foundation 22-14-00033 grant to A.B.

### Conflict of interest statement

The authors declare that the research was conducted in the absence of any commercial or financial relationships that could be construed as a potential conflict of interest. A.V. holds the position of Editorial Board Member for *Function* and was blinded from reviewing or making decisions for the manuscript.

### Data availability

The data underlying this article will be shared on reasonable request to the corresponding author.

### References

1. Semyanov A, Verkhratsky A. Inclusive brain: from neuronal doctrine to the active milieu. *Function* (Oxf). 2022;3(2):zqab069.
2. Semyanov A, Verkhratsky A. Astrocytic processes: from tripartite synapses to the active milieu. *Trends Neurosci*. 2021;44(10):781–792.
3. Kiehn O. Decoding the organisation of spinal circuits that control locomotion. *Nat Rev Neurosci*. 2016;17(4):224–238.
4. Buzsaki G. Large-scale recording of neuronal ensembles. *Nat Neurosci*. 2004;7(5):446–451.
5. Hubel DH, Wiesel TN. Receptive fields, binocular interaction and functional architecture in the cat's visual cortex. *J Physiol*. 1962;160(1):106–154.
6. Buzsaki G, McKenzie S, Davachi L. Neurophysiology of remembering. *Annu Rev Psychol*. 2022;73(1):187–215.
7. Shigetomi E, Kracun S, Sofroniew MV, Khakh BS. A genetically targeted optical sensor to monitor calcium signals in astrocyte processes. *Nat Neurosci*. 2010;13(6):759–766.
8. Chen TW, Wardill TJ, Sun Y, et al. Ultrasensitive fluorescent proteins for imaging neuronal activity. *Nature*. 2013;499(7458):295–300.
9. Rose CR, Verkhratsky A. Principles of sodium homeostasis and sodium signalling in astroglia. *Glia*. 2016;64(10):1611–1627.
10. Semyanov A, Henneberger C, Agarwal A. Making sense of astrocytic calcium signals—from acquisition to interpretation. *Nat Rev Neurosci*. 2020;21(10):551–564.

11. Kolenc OI, Quinn KP. Evaluating cell metabolism through autofluorescence imaging of NAD(P)H and FAD. *Antioxid Redox Signal*. 2019;**30**(6):875–889.
12. Popov A, Brazhe N, Fedotova A, et al. A high-fat diet changes astrocytic metabolism to promote synaptic plasticity and behavior. *Acta Physiol (Oxf)*. 2022;**236**(1):e13847.
13. Choquet D, Sainlos M, Sibarita JB. Advanced imaging and labelling methods to decipher brain cell organisation and function. *Nat Rev Neurosci*. 2021;**22**(4):237–255.
14. Tonnesen J, Inavalli V, Nagerl UV. Super-resolution imaging of the extracellular space in living brain tissue. *Cell*. 2018;**172**(5):1108–1121.e15.
15. Arizono M, Idziak A, Quici F, Nagerl UV. Getting sharper: the brain under the spotlight of super-resolution microscopy. *Trends Cell Biol*. 2023;**33**(2):148–161.
16. Whitaker M. Genetically encoded probes for measurement of intracellular calcium. *Methods Cell Biol*. 2010;**99**:153–182. Chapter 6.
17. Yu X, Nagai J, Khakh BS. Improved tools to study astrocytes. *Nat Rev Neurosci*. 2020;**21**(3):121–138.
18. Lin MZ, Schnitzer MJ. Genetically encoded indicators of neuronal activity. *Nat Neurosci*. 2016;**19**(9):1142–1153.
19. Hirase H, Qian L, Bartho P, Buzsaki G. Calcium dynamics of cortical astrocytic networks in vivo. *PLoS Biol*. 2004;**2**(4):E96.
20. Bojarskaite L, Bjørnstad DM, Pettersen KH, et al. Astrocytic  $\text{Ca}^{2+}$  signaling is reduced during sleep and is involved in the regulation of slow wave sleep. *Nat Commun*. 2020;**11**(1):3240.
21. Lines J, Martin ED, Kofuji P, Aguilar J, Araque A. Astrocytes modulate sensory-evoked neuronal network activity. *Nat Commun*. 2020;**11**(1):3689.
22. Dombeck DA, Khabbazi AN, Collman F, Adelman TL, Tank DW. Imaging large-scale neural activity with cellular resolution in awake, mobile mice. *Neuron*. 2007;**56**(1):43–57.
23. Royer S, Zemelman BV, Losonczy A, et al. Control of timing, rate and bursts of hippocampal place cells by dendritic and somatic inhibition. *Nat Neurosci*. 2012;**15**(5):769–775.
24. Thurley K, Ayaz A. Virtual reality systems for rodents. *Curr Zool*. 2017;**63**(1):109–119.
25. Doron A, Rubin A, Benmelech-Chovav A, et al. Hippocampal astrocytes encode reward location. *Nature*. 2022;**609**(7928):772–778.
26. Umpierre AD, Bystrom LL, Ying Y, et al. Microglial calcium signaling is attuned to neuronal activity in awake mice. *Elife*. 2020;**9**:e56502.
27. Kislin M, Mugantseva E, Molotkov D, et al. Flat-floored air-lifted platform: a new method for combining behavior with microscopy or electrophysiology on awake freely moving rodents. *J Vis Exp*. 2014;**(88)**:e51869.
28. van der Walt S, Schönberger JL, Nunez-Iglesias J, et al. scikit-image: image processing in Python. *PeerJ*. 2014;**2**:e453.
29. Virtanen P, Gommers R, Oliphant TE, et al. SciPy 1.0: fundamental algorithms for scientific computing in Python. *Nat Methods*. 2020;**17**(3):261–272.
30. Pnevmatikakis EA, Soudry D, Gao Y, et al. Simultaneous denoising, deconvolution, and demixing of calcium imaging data. *Neuron*. 2016;**89**(2):285–299.
31. Li CH, Tam PKS. An iterative algorithm for minimum cross entropy thresholding. *Pattern Recognit Lett*. 1998;**19**(8):771–776.
32. Seabold S, Perktold JS. Econometric and statistical modeling with python. *Proc of the 9th Python in Science Conf*. 2010;**2010**:92–96.
33. Tran CHT, Peringod G, Gordon GR. Astrocytes integrate behavioral state and vascular signals during functional hyperemia. *Neuron*. 2018;**100**(5):1133–1148.e3.
34. Mukamel EA, Nimmerjahn A, Schnitzer MJ. Automated analysis of cellular signals from large-scale calcium imaging data. *Neuron*. 2009;**63**(6):747–760.
35. Rungta RL, Bernier LP, Dissing-Olesen L, et al.  $\text{Ca}^{2+}$  transients in astrocyte fine processes occur via  $\text{Ca}^{2+}$  influx in the adult mouse hippocampus. *Glia*. 2016;**64**(12):2093–2103.
36. Wu YW, Gordleeva S, Tang X, et al. Morphological profile determines the frequency of spontaneous calcium events in astrocytic processes. *Glia*. 2019;**67**(2):246–262.
37. Giovannucci A, Friedrich J, Gunn P, et al. CalmAn an open source tool for scalable calcium imaging data analysis. *Elife*. 2019;**8**:e38173.
38. Semyanov A. Spatiotemporal pattern of calcium activity in astrocytic network. *Cell Calcium*. 2019;**78**:15–25.
39. Verkhratsky A, Semyanov A, Zorec R. Physiology of astroglial excitability. *Function (Oxf)*. 2020;**1**(2):zqaa016.
40. Lim D, Semyanov A, Genazzani A, Verkhratsky A. Calcium signaling in neuroglia. *Int Rev Cell Mol Biol*. 2021;**362**:1–53.
41. Oe Y, Wang X, Patriarchi T, et al. Distinct temporal integration of noradrenaline signaling by astrocytic second messengers during vigilance. *Nat Commun*. 2020;**11**(1):471.
42. Hertz L, Lovatt D, Goldman SA, Nedergaard M. Adrenoceptors in brain: cellular gene expression and effects on astrocytic metabolism and  $[\text{Ca}^{2+}]_i$ . *Neurochem Int*. 2010;**57**(4):411–420.
43. Ding F, O'Donnell J, Thrane AS, et al. Alpha1-adrenergic receptors mediate coordinated  $\text{Ca}^{2+}$  signaling of cortical astrocytes in awake, behaving mice. *Cell Calcium*. 2013;**54**(6):387–394.
44. Henneberger C, Papouin T, Oliet SH, Rusakov DA. Long-term potentiation depends on release of D-serine from astrocytes. *Nature*. 2010;**463**(7278):232–236.
45. Lind BL, Brazhe AR, Jessen SB, Tan FC, Lauritzen MJ. Rapid stimulus-evoked astrocyte  $\text{Ca}^{2+}$  elevations and hemodynamic responses in mouse somatosensory cortex in vivo. *Proc Natl Acad Sci USA*. 2013;**110**(48):E4678–E4687.
46. Horvat A, Muhić M, Smolić T, et al.  $\text{Ca}^{2+}$  as the prime trigger of aerobic glycolysis in astrocytes. *Cell Calcium*. 2021;**95**:102368.
47. Attwell D, Laughlin SB. An energy budget for signaling in the grey matter of the brain. *J Cereb Blood Flow Metab*. 2001;**21**(10):1133–1145.
48. Brini M, Cali T, Ottolini D, Carafoli E. Neuronal calcium signaling: function and dysfunction. *Cell Mol Life Sci*. 2014;**71**(15):2787–2814.
49. Ghosh A, Greenberg ME. Calcium signaling in neurons: molecular mechanisms and cellular consequences. *Science*. 1995;**268**(5208):239–247.
50. Sherwood MW, Arizono M, Panatier A, Mikoshiba K, Oliet SHR. Astrocytic  $\text{IP}_3\text{Rs}$ : beyond  $\text{IP}_3\text{R2}$ . *Front Cell Neurosci*. 2021;**15**:695817.
51. Rose J, Brian C, Pappa A, Panayiotidis MI, Franco R. Mitochondrial metabolism in astrocytes regulates brain bioenergetics, neurotransmission and redox balance. *Front Neurosci*. 2020;**14**:536682.
52. Lopez-Fabuel I, Le Douce J, Logan A, et al. Complex I assembly into supercomplexes determines differential mitochondrial ROS production in neurons and astrocytes. *Proc Natl Acad Sci USA*. 2016;**113**(46):13063–13068.



53. Zhao RZ, Jiang S, Zhang L, Yu ZB. Mitochondrial electron transport chain, ROS generation and uncoupling (review). *Int J Mol Med*. 2019;**44**(1):3–15.
54. Knapp LT, Klann E. Potentiation of hippocampal synaptic transmission by superoxide requires the oxidative activation of protein kinase C. *J Neurosci*. 2002;**22**(3):674–683.
55. Stobart JL, Ferrari KD, Barrett MJP, et al. Long-term in vivo calcium imaging of astrocytes reveals distinct cellular compartment responses to sensory stimulation. *Cereb Cortex*. 2018;**28**(1):184–198.
56. Salmon CK, Syed TA, Kacerovsky JB, et al. Organising principles of astrocytic nanoarchitecture in the mouse cerebral cortex. *Curr Biol*. 2023;**33**(5):957–972.e5.
57. Stuart GJ, Spruston N. Dendritic integration: 60 years of progress. *Nat Neurosci*. 2015;**18**(12):1713–1721.
58. Clapham DE. Calcium signaling. *Cell*. 2007;**131**(6):1047–1058.
59. Rizzuto R, De Stefani D, Raffaello A, Mammucari C. Mitochondria as sensors and regulators of calcium signalling. *Nat Rev Mol Cell Biol*. 2012;**13**(9):566–578.
60. Glancy B, Willis WT, Chess DJ, Balaban RS. Effect of calcium on the oxidative phosphorylation cascade in skeletal muscle mitochondria. *Biochemistry*. 2013;**52**(16):2793–2809.
61. Pasti L, Volterra A, Pozzan T, Carmignoto G. Intracellular calcium oscillations in astrocytes: a highly plastic, bidirectional form of communication between neurons and astrocytes in situ. *J Neurosci*. 1997;**17**(20):7817–7830.
62. Pasti L, Pozzan T, Carmignoto G. Long-lasting changes of calcium oscillations in astrocytes. A new form of glutamate-mediated plasticity. *J Biol Chem*. 1995;**270**(25):15203–15210.
63. Cornell-Bell AH, Finkbeiner SM, Cooper MS, Smith SJ. Glutamate induces calcium waves in cultured astrocytes: long-range glial signaling. *Science*. 1990;**247**(4941):470–473.
64. Verisokin AY, Verveiko DV, Postnov DE, Brazhe AR. Modeling of astrocyte networks: toward realistic topology and dynamics. *Front Cell Neurosci*. 2021;**15**:645068.
65. Ullah G, Jung P, Cornell-Bell AH. Anti-phase calcium oscillations in astrocytes via inositol (1, 4, 5)-trisphosphate regeneration. *Cell Calcium*. 2006;**39**(3):197–208.
66. Dupont G, Combettes L, Bird GS, Putney JW. Calcium oscillations. *Cold Spring Harb Perspect Biol*. 2011;**3**(3):a004226.
67. Smedler E, Uhlen P. Frequency decoding of calcium oscillations. *Biochim Biophys Acta*. 2014;**1840**(3):964–969.